




Curing Mechanism and Mechanical Properties of Al₂O₃/Cyanate Ester–Epoxy Composites

YUFEI CHEN ^{1,2,4} ZHIGUO LI,^{1,5} YULONG LIU,^{1,6} CHENGJUN TENG,^{3,7}
and WEIWEI CUI^{1,8}

1.—School of Materials Science and Engineering, Harbin University of Science and Technology, Harbin 150040, China. 2.—Key Laboratory of Engineering Dielectrics and Its Application, Harbin University of Science and Technology, Ministry of Education, Harbin 150080, China. 3.—Harbin Xiangfang District Center for Disease Control and Prevention, Harbin 150030, China. 4.—e-mail: chen yufei@hrbust.edu.cn. 5.—e-mail: lizhiguomy@gmail.com. 6.—e-mail: 375976129@qq.com. 7.—e-mail: 810025406@qq.com. 8.—e-mail: cuiww@hrbust.edu.cn

Bisphenol A epoxy resin (E51) and biscyanatophenylpropane (BCE) as polymer matrix and aluminum oxide (Al₂O₃, self-made by sol–gel method) as modification agent have been used to prepare two-phase Al₂O₃/E51–BCE composites for application in various fields. The curing process and kinetics of the system were determined by nonisothermal differential scanning calorimetry. The average apparent activation energy of the system calculated by the Kissinger and Ozawa methods was 67.8 kJ/mol. Scanning electron microscopy revealed that the interface between the Al₂O₃ phase and E51–BCE matrix phase was blurred and displayed mutual penetration. The fracture morphology of the Al₂O₃/E51–BCE composites exhibited ductile fracture. Al₂O₃ phase was uniformly dispersed in the matrix resin. The bending strength, bending modulus, and impact strength of the Al₂O₃/E51–BCE composites showed peak values of 172.3 MPa, 2.5 GPa, and 24.2 kJ/m², being 24.4%, 19.1%, and 53.2% higher compared with the matrix resin, respectively, when the Al₂O₃ content was 3 wt.%.

Key words: Biscyanatophenylpropane, epoxy resin, curing kinetics, micromorphology, mechanical properties

INTRODUCTION

The structure of cyanate ester (CE) resin contains two or more cyanate groups with high activity, which can form a triazine that results in a highly cross-linked network with a trimerization structure under the action of heat or a catalyst. These macromolecules provide CE resin with good mechanical properties and strong heat resistance,^{1–4} having current applications in electronics packaging, aerospace structural components, adhesives, and missile materials.^{5–8} However, the triazine ring structure of the CE molecule is highly symmetrical, easy to crystallize, and brittle, making

improvement of its toughness an urgent problem.^{9–13}

Epoxy resin is a kind of thermosetting resin with strong reaction activity and wide applications,^{14–16} being commonly used to toughen cyanate resin.^{17,18} Nanoscale aluminum oxide (Al₂O₃) shows interfacial and small size effects, which can help to improve the mechanical properties of composites.^{19–23}

There are few reports on the mechanical properties of cyanate resin modified by nanoscale Al₂O₃. Based on previous studies, the reaction mechanism of cyanate ester with epoxy resin was studied in detail. Nanoscale Al₂O₃ self-made by a sol–gel method was used as reinforcement, and the Al₂O₃/E51–BCE composite was prepared by a bulk polymerization method. Then, the mechanical properties of the composites were analyzed to explore the

(Received June 20, 2019; accepted November 14, 2019; published online November 27, 2019)

effects of the nanoscale Al_2O_3 on the material. The results provide a reference for preparation of high-performance materials and broaden the application fields of cyanate ester resin.

EXPERIMENTAL PROCEDURES

Materials

Biscyanatophenylpropane (BCE) was purchased from Yangzhou Technical Material Co. Ltd. Bisphenol A epoxy resin (E51, epoxy value 0.51) was an industrial product provided by Bluestar New Chemical Materials. Aluminum isopropoxide (chemically pure) was from Tianjin Fuchen Chemical reagent factory. Isopropanol (analytical pure) was from Dongguan Spartan Reagent Co., Ltd.

Preparation of Al_2O_3

Aluminum isopropoxide, isopropanol, and deionized water were mixed in a water bath at 353 K for 2 h to sufficiently hydrolyze aluminum isopropoxide. The isopropanol and deionized water were removed by distillation under reduced pressure, and the solid was dried at 393 K and calcined at 973 K for 3 h to obtain Al_2O_3 .

Synthesis of E51-BCE

The mass ratio of E51 to BCE was set to 2:8. E51 was preheated to 363 K, and BCE was added into E51. Then, the mixed system was heated to 388 K and kept for 1 h. After that, the mixed system was poured into a mold which had been preheated to 413 K and cured at 453 K for 4 h then 473 K for 2 h to obtain the modified cyanate material (E51-BCE).

Preparation of Al_2O_3 /E51-BCE Composite Materials

Al_2O_3 was added into E51 and ultrasonically dispersed for 0.5 h at 353 K. BCE was added into above system to prepare Al_2O_3 /E51-BCE composites, according to the 453 K/4 h + 473 K/2 h procedure. The sample names along with their components are presented in Table I.

Measurements

Differential scanning calorimetry (DSC) measurements were carried out using a DSC6220 under a constant flow of nitrogen to study the curing process

Table I. Samples and their components

Sample no.	Components	Al_2O_3 content/wt.%
A0	E51-BCE	0
A1	Al_2O_3 /E51-BCE	1
A2	Al_2O_3 /E51-BCE	3
A3	Al_2O_3 /E51-BCE	5

and reaction kinetics at heating rates of 5 K/min, 10 K/min, 15 K/min, and 20 K/min.

Fourier-transform infrared (FT-IR) spectrometry (EQUINOX-55, Germany) in the range of 400 cm^{-1} to 4000 cm^{-1} was used to track the chemical reactions during the curing process and to study the chemical structure of the materials.

The fracture micromorphology of the samples was observed by scanning electron microscopy (SEM) using a Hitachi 4300 (Philips, The Netherlands). The samples were deposited on a sample holder with adhesive carbon foil and sputtered with gold before examination.

The micromorphology of Al_2O_3 was characterized by transmission electron microscopy (TEM, JEM-2100; JEOL, Japan).

The impact strength of the composite materials was measured using a Charpy impact tester (TCJ-4, Jinan Huaxing Laboratory Equipment, China) according to native standard GB/T 2567-2008. The length, width, and thickness of the sample was $80 \pm 0.5\text{ mm}$, $10 \pm 0.1\text{ mm}$, and $4 \pm 0.1\text{ mm}$, respectively. For each sample, five measurements were made and the average value taken.

The bending strength and bending modulus of the samples were determined by using an electronic testing machine (CSS-4430, Shanghai Technical Instrument, China) according to the native standard GB/T 2918-1998. The length, width, and thickness of the sample was $80 \pm 0.5\text{ mm}$, $10 \pm 0.1\text{ mm}$, and $4 \pm 0.1\text{ mm}$, respectively, and the span was 60 mm at a speed of 2 mm/min.

RESULTS AND DISCUSSION

Curing Process of E51-BCE

Figure 1 and Table II show the nonisothermal DSC curves and characteristic temperatures of the curing system at the different heating rates. It can be seen from Fig. 1 that the peak temperature of the

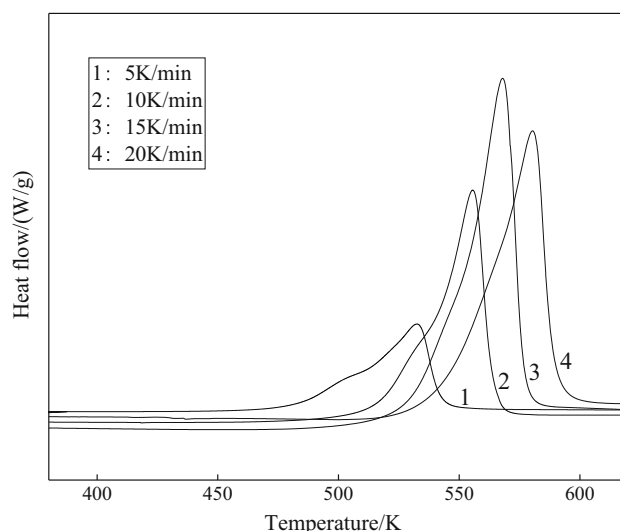


Fig. 1. DSC curves of E51-BCE system.

Table II. DSC data of curing system. T_i , initial curing temperature; T_p , peak temperature; T_f , terminal curing temperature

Heating rate, β (K min ⁻¹)	T_i (K)	T_p (K)	T_f (K)
5	451	532	569
10	480	556	570
15	505	568	593
20	519	580	618

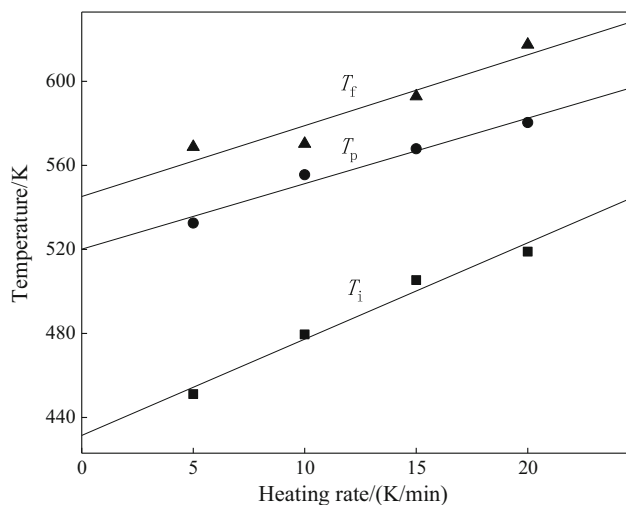
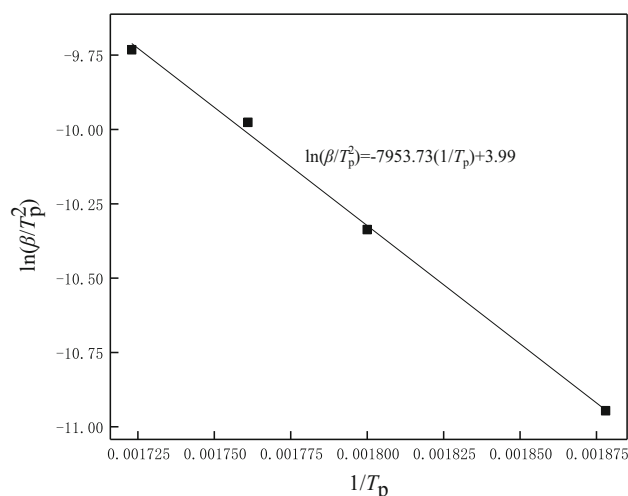
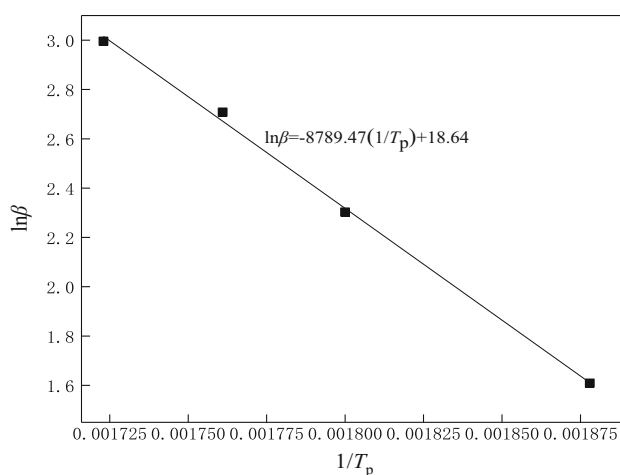


Fig. 2. Relationship between characteristic temperatures and heating rate of E51–BCE system.

exothermic reaction gradually shifted toward higher values with increasing heating rate. A weak exothermic reaction peak was observed at 508 K when the heating rate was 5 K/min, gradually disappearing with increase of the heating rate. Finally, a single exothermic peak formed, indicating the occurrence of multiple reactions in the curing system and the overlap between two or more exothermic reaction peaks.

Based on the results presented in Table II, the characteristic temperature can be extrapolated to a heating rate of 0 K/min by using the linear fitting method (Fig. 2), yielding characteristic T_i , T_p , and T_f temperatures of 431 K, 520 K, and 545 K, respectively.

Based on the time–temperature equivalence principle, the system will react completely in a short time under high-temperature conditions. However, the movement of the molecular chains is hindered and the reaction rate decreases with the increasing degree of polymerization during the reaction, resulting in an incomplete reaction. Based on the analysis above, the curing process was finally determined to be 453 K/4 h + 473 K/2 h.

Fig. 3. Relationship between $\ln(\beta/T_p^2)$ and $1/T_p$ of E51–BCE system.Fig. 4. Relationship between $\ln\beta$ and $1/T_p$ of E51–BCE system.

Curing Kinetics of E51–BCE

To make the calculation results more reasonable, two methods are usually used to calculate the apparent activation energy, viz. the Kissinger method (Eq. 1) and Ozawa method (Eq. 2)^{24–26}:

$$\ln\left(\frac{\beta}{T_p^2}\right) = \ln\left(\frac{AR}{E_a}\right) - \frac{E_a}{R} \frac{1}{T_p}, \quad (1)$$

$$E_a = \frac{-R}{1.052} \frac{d \ln \beta}{d\left(\frac{1}{T_p}\right)}. \quad (2)$$

In both equations, β is the heating rate [K min⁻¹], T_p is the peak temperature [K], R is the molar gas constant ($R = 8.314 \text{ J mol}^{-1} \text{ K}^{-1}$), E_a is the apparent activation energy, and A is the preexponential

factor. In Eq. 1, the apparent activation energy E_a can be obtained by linearly fitting $\ln(\beta/T_p^2)$ versus $1/T_p$ (Fig. 3). And in Eq. 2, E_a can also be calculated by linearly fitting $\ln\beta$ versus $1/T_p$ (Fig. 4). Finally, the apparent activation energy E_a is calculated to be 66.2 kJ/mol by the Kissinger method and 69.5 kJ/mol by the Ozawa method. The values calculated by these two methods are close to each other, and the reaction system is reasonable. The average value of the apparent activation energy of 67.8 kJ/mol is thus taken. By transforming the Kissinger method, A can be calculated using Eq. 3:

$$A = \frac{\beta E_a \exp(E_a/RT_p)}{RT_p^2}. \quad (3)$$

According to the Crane law (Eq. 4) and Arrhenius law (Eq. 5),^{27–29} the order of reaction and the reaction rate constant can be calculated using the following equations, respectively:

$$\frac{d(\ln\beta)}{d(1/T_p)} = -\frac{E_a}{nR}, \quad (4)$$

$$\ln k = -E_a/RT + \ln A, \quad (5)$$

where n is the order of reaction, T is the reaction temperature, and k is the reaction rate constant. According to the results of linearly fitting $\ln\beta$ versus $1/T_p$, the reaction order n is about $0.91 \approx 1$, indicating that the curing system is close to a first-order reaction. The calculation results for the reaction kinetic parameters are presented in Table III.

Curing Reaction Mechanism of E51–BCE

The possible polymerizations of the E51–BCE system are shown in Fig. 5. Cyanate groups react with epoxides to form oxazoline in Scheme 1. Scheme 2 presents self-polymerizations of cyanate ester, while Scheme 3 displays the process for ring-opening reaction of triazine ring and epoxy resin to form oxazolidinone. The infrared characteristic absorption peaks of E51–BCE are presented in Table IV.

To verify the curing reaction mechanism of the E51–BCE system, FT-IR spectroscopy was used to study the curing process with initial temperatures of 433 K and 453 K. Figure 6 presents the FT-IR

spectra of E51–BCE material at 433 K/1 h, 443 K/1 h, and 453 K/10 min. It can be seen from Fig. 6 that the characteristic absorption peak of triazine ring appears at 1564 cm^{-1} (433 K for 1 h), and the oxazoline characteristic absorption peak appears at 1680 cm^{-1} too, indicating that the cyanate groups not only undergo self-polymerization to form triazine rings at 433 K, but also react with epoxides to form oxazoline structures. At this time, the Scheme 2 reaction and the Scheme 1 reaction occur simultaneously in the system. After curing at 443 K for 1 h, the intensity of the absorption peak at 2270 cm^{-1} is weakened, indicating that the cyanate ester continues to react. At the same time, an absorption peak characteristic of oxazolidinone appears at 1770 cm^{-1} , which is due to Scheme 3, indicating that oxazoline and oxazolidinone coexist in the system. After curing at 453 K for 10 min, the absorption peak at 2270 cm^{-1} weakens rapidly while the absorption peak at 915 cm^{-1} becomes weaker, indicating that the cyanate ester is mainly consumed in the reaction of Scheme 2.

Figure 7 displays the FT-IR spectra of E51–BCE material at the initial curing temperature of 453 K, to observe the change of the absorption peak and track the process of the curing reaction from 10 min to 60 min. At the condition 453 K/20 min, the absorption peaks at 2270 cm^{-1} and 915 cm^{-1} are not significantly weakened, indicating that the speed of the reaction between cyanate ester and epoxy resin is still low. After curing at 453 K for 30 min, the absorption peak at 915 cm^{-1} starts to weaken and weak absorption peaks appear at 1564 cm^{-1} and 1680 cm^{-1} , corresponding to the structure of triazine ring and oxazoline, respectively. Therefore, Scheme 1 and Scheme 2 occur simultaneously in the system. The intensity of the peak at 1564 cm^{-1} is obviously higher than that at 1680 cm^{-1} , indicating that the main reaction occurring in the system is trimeric ring formation of cyanate ester, while a little amount of cyanate ester reacts with epoxy resin to form the oxazoline structure. When the curing time is 40 min to 60 min, the absorption peaks at 2270 cm^{-1} and 915 cm^{-1} weakened, the absorption peak at 1564 cm^{-1} was enhanced, and the intensity of the absorption peak at 1680 cm^{-1} increased slightly. These results indicate that the reaction of cyanate trimerization ring accelerated at 453 K, while the

Table III. Reaction kinetic parameters of E51–BCE curing system

E_a (kJ/mol)	A ($\times 10^8$)		k
	Calculation results	Average value	
67.8	4.3	4.3	$k_1: 1.1 \times 10^{-6}$ (298 K) $k_2: 1.0 \times 10^{-2}$ (453 K) $k_3: 2.1 \times 10^{-2}$ (473 K)
	4.3		
	4.5		
	4.2		

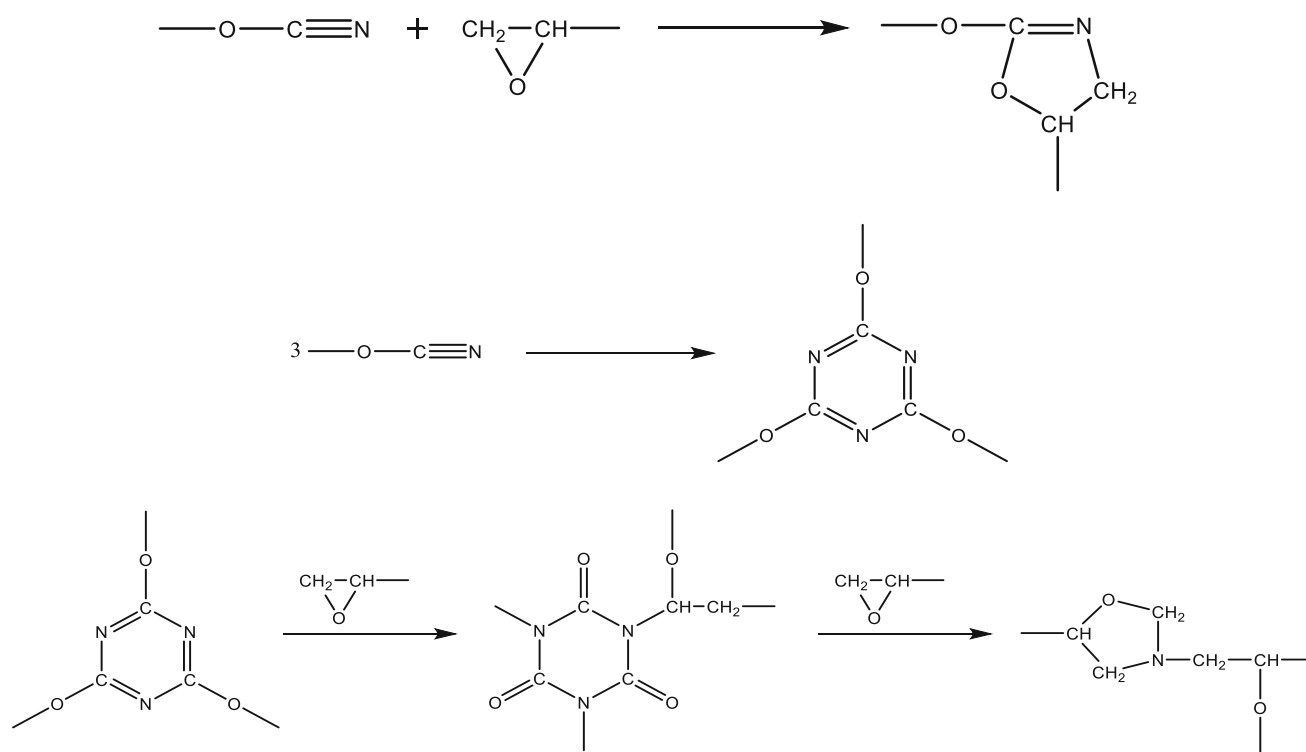


Fig. 5. Possible polymerizations of E51-BCE curing system.

Table IV. Characteristic infrared absorption peaks of E51-BCE material

ν (cm ⁻¹)	2270	1770	1680	1564	915
Chemical group	-OCN	-C=O	>C=N-	N-C=N	Epoxy

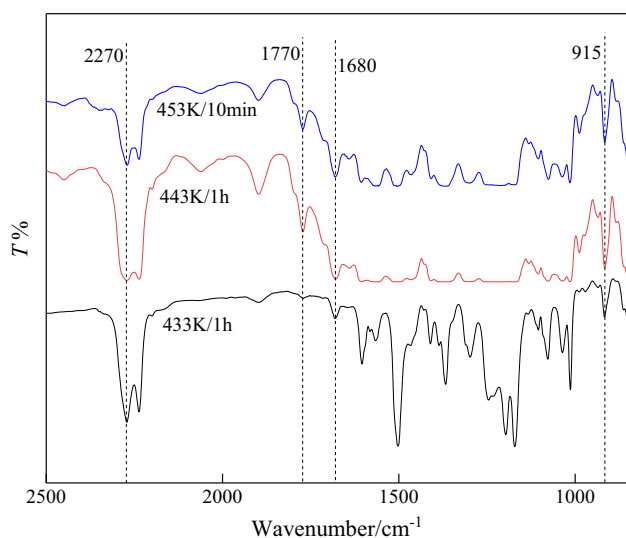


Fig. 6. FT-IR spectra of E51-BCE material at initial curing temperature of 433 K.

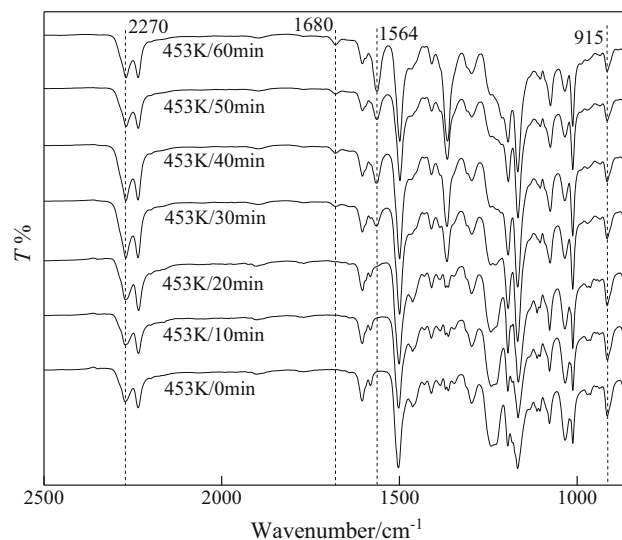


Fig. 7. FT-IR spectra of E51-BCE system for different curing time at initial curing temperature of 453 K.

reaction rate between the cyanate ester and the epoxy resin became slow. The reaction of Scheme 2 occurs mainly in the system.

It can also be seen from Fig. 7 that the oxazolidinone absorption peak does not appear at 1770 cm⁻¹ after curing at 453 K/60 min, and the oxazoline

absorption peak also weakens. In Fig. 6, the oxazolidinone absorption peak appears when cured at 443 K for 1 h, and the intensity of the absorption peak at 1770 cm^{-1} is not enhanced after curing at 453 K for 10 min. Therefore, it can be considered that the reactivity ratio of the cyanate ester to epoxy resin is higher, while the reactivity ratio of self-polymerization is lower, when the initial curing temperature is low. The cyanate ester is mostly consumed in the reaction with the epoxy resin. When the initial curing temperature is above 453 K, the cyanate ester mainly undergoes self-polymerization to form a triazine ring, and the reaction rate is fast. A small amount of cyanate ester reacts with the epoxy resin to form oxazoline structures.

Micromorphology of Al_2O_3 and $\text{Al}_2\text{O}_3/\text{E51-BCE}$ Composites

Figure 8 presents the FT-IR spectra of Al_2O_3 , E51-BCE, and $\text{Al}_2\text{O}_3/\text{E51-BCE}$, while TEM images of Al_2O_3 are exhibited in Fig. 9. Figure 8 shows that the self-made Al_2O_3 exhibited infrared absorption peaks at 3725 cm^{-1} and 3697 cm^{-1} , which are characteristic of hydroxyl group. The intensity of the two absorption peaks was weak, indicating that the surface of Al_2O_3 contained a small amount of hydroxyl group, which can be beneficial to improve the interaction with the polymer matrix. E51-BCE and $\text{Al}_2\text{O}_3/\text{E51-BCE}$ both exhibited infrared absorption peaks at 1210 cm^{-1} (C-O-C) and 1070 cm^{-1} (C-O-C, C-O), corresponding to the ether bond formed by the curing reaction of E51 and BCE.³⁰ It can be seen from Fig. 9 that the Al_2O_3 was in the form of short fiber-like crystals of nanometer size, a structure that can improve the mechanical properties of the composite material and meet the application requirements.

To observe the dispersal state of the Al_2O_3 inside the E51-BCE matrix and the fracture surface

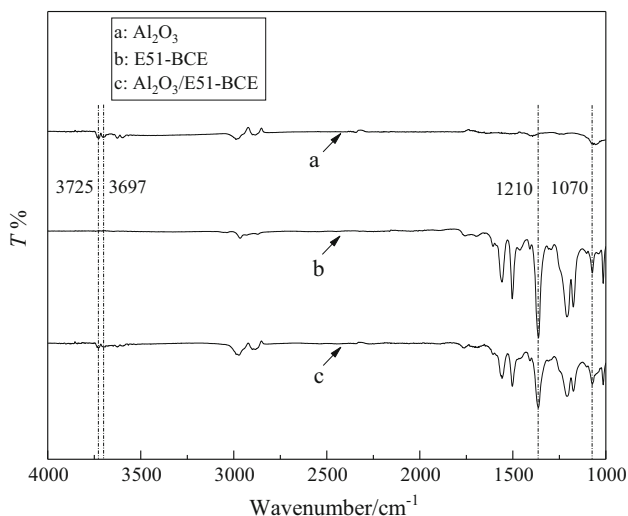


Fig. 8. FT-IR spectra of Al_2O_3 , E51-BCE, and $\text{Al}_2\text{O}_3/\text{E51-BCE}$.

morphology of the $\text{Al}_2\text{O}_3/\text{E51-BCE}$ composites, the fracture surfaces of E51-BCE, 1 wt.% $\text{Al}_2\text{O}_3/\text{E51-BCE}$, 3 wt.% $\text{Al}_2\text{O}_3/\text{E51-BCE}$, and 5 wt.% $\text{Al}_2\text{O}_3/\text{E51-BCE}$ were characterized by SEM; the resulting images are presented in Fig. 10a, b, c, and d. From Fig. 10a, it can be seen that the fracture surface of E51-BCE was basically regular and smooth, while the broken cracks indicate single-directional dendritic development, which basically conforms with a brittle fracture characteristic. This is because the internal structure of the resin is very regular when the material is subjected to external forces, and there is no obstruction. Therefore, the cracks expand in one direction, with both the external force and internal structure making the cracks progress smoothly along the stress direction. In Fig. 10b-d, the fracture surface morphology of the composites is different from that seen in Fig. 10a due to the existence of the Al_2O_3 component, with irregular cracks appearing. The fracture surface of the composites exhibited short and disorderly cracks when the content of Al_2O_3 reached 3 wt.%, as shown in Fig. 10c. The morphology is a typical two-phase structure, with E51-BCE phase (dark areas, continuous phase) as the matrix and Al_2O_3 phase (bright areas, dispersed phase) as the reinforcement. The Al_2O_3 was dispersed evenly in the continuous phase, and the strong interaction makes the crack directions of the composite materials change and present arborization when the material is subjected to an external force, resulting in ductile fracture behavior. Many microcracks and silver streaks formed and absorb the fracture energy, and shear zones are induced by Al_2O_3 particles when the interaction between the two phases is stronger. Based on Fig. 10d, the scale of Al_2O_3 increases and its agglomeration is enhanced, weakening the interaction between Al_2O_3 and the matrix resin, which indicates that excess Al_2O_3 will not be beneficial to improve the composite material.

Mechanical Properties of $\text{Al}_2\text{O}_3/\text{E51-BCE}$ Composites

The bending strength, bending modulus, and impact strength of composites are important indicators of their mechanical properties. The experimental results for the $\text{Al}_2\text{O}_3/\text{E51-BCE}$ composites are presented in Table V, demonstrating that the bending strength, bending modulus, and impact strength of sample A2 showed the peak values of 172.3 MPa, 2.5 GPa, and 24.2 kJ/m^2 , being 24.4%, 19.1%, and 53.2% higher than those of the matrix resin, respectively. The main reasons may be that the interaction of the Al_2O_3 and E51-BCE matrix can prevent the spread of fractional fissures, change their direction, and absorb fracture energy when the composite is subjected to an external force. The mechanical properties of the composites increased as the content of Al_2O_3 was increased. On the other hand, the two-phase structure consisting of Al_2O_3 in

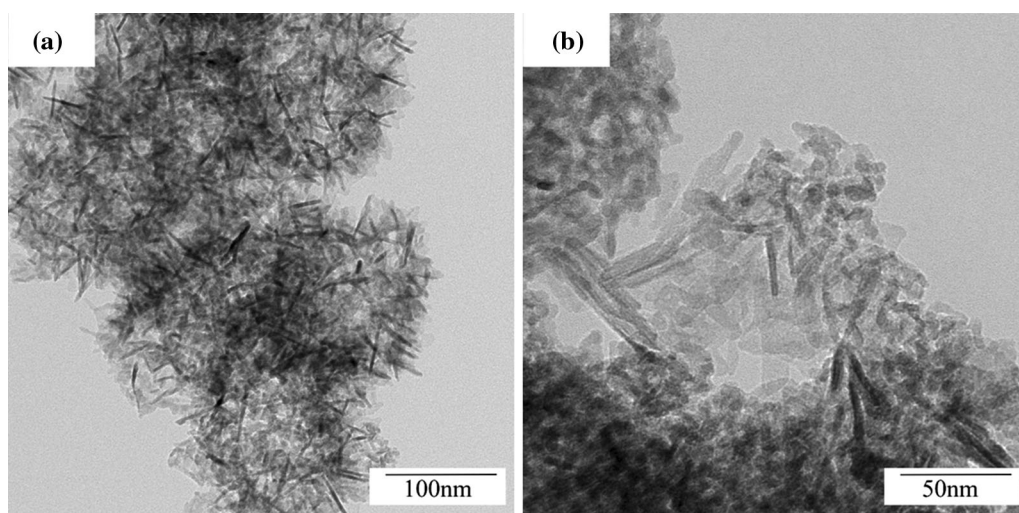


Fig. 9. TEM images of Al₂O₃ at (a) 40,000 \times and (b) 100,000 \times .

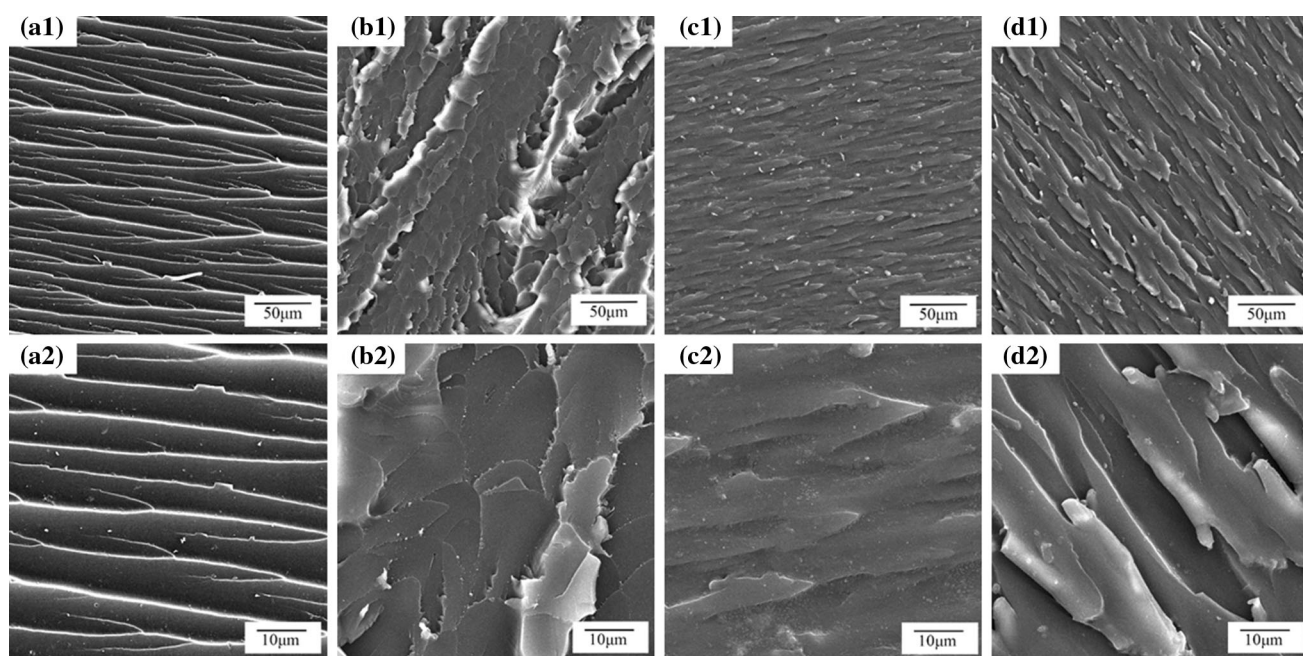


Fig. 10. SEM images of Al₂O₃/E51–BCE composites: (a1, a2) E51–BCE, (b1, b2) 1 wt.% Al₂O₃/E51–BCE, (c1, c2) 3 wt.% Al₂O₃/E51–BCE, and (d1, d2) 5 wt.% Al₂O₃/E51–BCE.

the E51–BCE matrix can play the role of a bridge, and a good interface forms, which can hinder the spread of fissures when the composite is subject to an external force. The direction of the fissure changes and it develops from the interface to all around, while micropores will be formed, absorbing lots of energy in the process, while Al₂O₃ resists failure cracks, so the crack tips become blunt and broken cracks do not extend easily. Furthermore, the mechanical properties decrease when the content of Al₂O₃ is too high, as the scale of the Al₂O₃ particles will increase, their dispersion in the E51–BCE matrix will reduce, and the interfacial interaction will weaken. Obvious gaps appear in the

interface microarea, and broken cracks pass smoothly through Al₂O₃ particles, thus degrading the mechanical properties. This is confirmed by the discussion above of the microstructure. Also, the oxazolidinone structure formed by the reaction of E51 and BCE is linked to the triazine ring by an ether bond, which is longer and can exhibit internal rotation, thus improving the flexibility of the molecular chain and thereby the toughness of the material.³¹ Since the hydroxyl groups on the surface of Al₂O₃ react with the epoxy group at high temperature, the amount of ether bonds in the material is reduced and the content of the soft segment of the composites is lowered, as confirmed in Fig. 8. Due to

Table V. Bending strength, bending modulus, and impact strength of Al₂O₃/E51–BCE composites

Sample	Components	Bending strength		Bending modulus		Impact strength	
		Value (MPa)	Increase ratio (%)	Value (GPa)	Increase ratio (%)	Value (kJ/m ²)	Increase ratio (%)
A0	E51–BCE	138.6		2.1		15.8	
A1	1 wt.% Al ₂ O ₃ /E51–BCE	146.8	8.2	2.4	14.3	22.6	43.0
A2	3 wt.% Al ₂ O ₃ /E51–BCE	172.3	24.4	2.5	19.1	24.2	53.2
A3	5 wt.% Al ₂ O ₃ /E51–BCE	155.2	16.6	2.2	4.8	20.1	27.2

The increase ratio for samples A1, A2, and A3 is in comparison with A0.

the low hydroxyl content of the Al₂O₃ surface, this effect is not obvious when the content of Al₂O₃ is low. The number of ether bonds is obviously lower, giving rise to a decrease in the impact strength of the composites when the Al₂O₃ content is more than 3 wt.%.

CONCLUSIONS

- The curing process of E51–BCE was determined by nonisothermal DSC to be 453 K/2 h + 473 K/2 h. The apparent activation energy was calculated to be 66.1 kJ/mol and 69.5 kJ/mol by the Kissinger method and Ozawa method, respectively, with an average value of 67.8 kJ/mol. The reaction rate constants of the system are 1.1×10^{-6} at 298 K, 1.0×10^{-2} at 453 K, and 2.1×10^{-2} at 473 K.
- When the curing temperature was below 453 K, the rate of cyanate ester self-polymerization was slow and the reaction probability between epoxy resin and cyanate was high. Cyanate tends to self-polymerize and form triazine ring, then reacts with epoxy, decreasing the probability of epoxy resin reacting directly with the cyanate ester, when the temperature is above 453 K.
- The Al₂O₃ prepared by the sol–gel method was a short fiber-like crystal with nanosize, having a small amount of hydroxyl groups on its surface. When the content of Al₂O₃ was 3 wt.%, the Al₂O₃ was well dispersed in the E51–BCE matrix resin, and ductile fracture was observed.
- Introduction of Al₂O₃ significantly improved the mechanical properties of Al₂O₃/E51–BCE composites. The bending strength, bending modulus, and impact strength of the Al₂O₃/E51–BCE composites reached their highest values of 172.3 MPa, 2.5 GPa, and 24.2 kJ/m², being 24.4%, 19.1% and 53.2% higher than that of the matrix resin, respectively, when the Al₂O₃ content was 3 wt.%.

ACKNOWLEDGMENTS

Funding was provided by the National Natural Science Foundation of China (Grant No. 21604019) and Harbin technology bureau subject leader (Grant No. 2015RAXXJ029).

CONFLICT OF INTEREST

The author(s) declare no potential conflicts of interest with respect to the research, authorship, and/or publication of this article.

REFERENCES

- S. Zhang, Y.H. Yan, X.D. Li, H.J. Fan, Q.C. Ran, Q. Fu, and Y. Gu, *Eur. Polym. J.* 103, 124 (2018).
- Y. Lin and M. Song, *React. Funct. Polym.* 129, 58 (2018).
- S.H. Wang, Y.P. Tu, L.Z. Fan, C.Q. Yi, Z.X. Wu, and L.F. Li, *J. Phys. D-Appl. Phys.* (2018). <https://doi.org/10.1088/1361-6463/aaaa01>.
- J.X. Ma, X.F. Lei, Y.H. Wang, and Y.Y. Sun, *Iran. Polym. J.* 27, 145 (2018).
- Y.Q. Wang, S.Y. Zhou, and H.Y. Du, *J. Mater. Sci.-Mater. Electron.* 29, 12360 (2018).
- Y.S. Tang, W.C. Dong, L. Tang, Y.K. Zhang, J. Kong, and J.W. Gu, *Compos. Commun.* 8, 36 (2018).
- C.Q. Lu, L. Yuan, Q.B. Guan, G.Z. Liang, and A.J. Gu, *J. Phys. Chem. C* 122, 5238 (2018).
- G.L. Wu, Y.H. Cheng, K.K. Wang, Y.Q. Wang, and A.L. Feng, *J. Mater. Sci.-Mater. Electron.* 27, 5592 (2016).
- L. Yuan, G.Z. Liang, and A.J. Gu, *Polym. Degrad. Stabil.* 96, 84 (2011).
- L. Tang, J. Dang, M.K. He, J.Y. Li, J. Kong, Y.S. Tang, and J.W. Gu, *Compos. Sci. Technol.* 169, 120 (2019).
- C. Uhlig, M. Bauer, J. Bauer, O. Kahle, A.C. Taylor, and A.J. Kinloch, *React. Funct. Polym.* 129, 2 (2018).
- A. Inamdar, J. Cherukattu, A. Anand, and B. Kandasubramanian, *Ind. Eng. Chem. Res.* 57, 4479 (2018).
- A. Zegaoui, M. Derradji, R.K. Ma, W.A. Cai, W.B. Liu, J. Wang, A.Q. Dayo, S. Song, and L.L. Zhang, *J. Appl. Polym. Sci.* (2018). <https://doi.org/10.1002/app.46283>.
- Z.D. Wang, M.M. Yang, Y.H. Cheng, J.Y. Liu, B. Xiao, S.Y. Chen, J.L. Huang, Q. Xie, G.L. Wu, and H.J. Wu, *Compos. Pt. A-Appl. Sci. Manuf.* 118, 302 (2019).
- S.Y. Chen, Y.H. Cheng, Q. Xie, B. Xiao, Z.D. Wang, J.Y. Liu, and G.L. Wu, *Compos. Pt. A-Appl. Sci. Manuf.* 120, 84 (2019).
- Z.R. Jia, Z.G. Gao, D. Lan, Y.H. Cheng, G.L. Wu, and H.J. Wu, *Chin. Phys. B* (2018). <https://doi.org/10.1088/1674-1056/27/11/117806>.
- F. Wu, B. Song, J. Hah, C.C. Tuan, K.S. Moon, and C.P. Wong, *J. Polym. Sci. Polym. Chem.* 56, 2412 (2018).

18. F. Wu, C.C. Tuan, B. Song, K.S. Moon, and C.P. Wong, *J. Polym. Sci. Polym. Chem.* 56, 1337 (2018).
19. S. Yazman and A. Samanci, *Arab. J. Sci. Eng.* 44, 1353 (2019).
20. L. Pan, W.Y. Ding, W.L. Ma, J.L. Hu, X.F. Pang, F. Wang, and J. Tao, *Mater. Des.* 160, 1106 (2018).
21. J.M. Fan and S.A. Xu, *Iran. Polym. J.* 27, 339 (2018).
22. P.T.R. Swain and S. Biswas, *J. Compos. Mater.* 51, 3909 (2017).
23. A. Permal, M. Devarajan, H.L. Huang, T. Zahner, D. Lacey, and K. Ibarhim, *J. Mater. Sci.-Mater. Electron.* 28, 13487 (2017).
24. Y. Zhang, L. Yuan, F. Chen, A.J. Gu, and G.Z. Liang, *Polym. Bull.* 74, 1011 (2017).
25. X.L. Zeng, S.H. Yu, and R. Sun, *J. Therm. Anal. Calorim.* 114, 387 (2013).
26. R.Y. Ghumara, P.P. Adroja, and P.H. Parsania, *J. Therm. Anal. Calorim.* 114, 873 (2013).
27. G.M. Wu, Z.W. Kong, C.F. Chen, J. Chen, S.P. Huo, and J.C. Jiang, *J. Therm. Anal. Calorim.* 111, 735 (2013).
28. Y. Liu, J. Wang, and S.A. Xu, *J. Polym. Sci. Polym. Chem.* 52, 472 (2014).
29. C. Alzina, N. Sbirrazzuoli, and A. Mija, *J. Phys. Chem. B* 114, 12480 (2010).
30. F. Ren, G.M. Zhu, P.G. Ren, Y.K. Wang, and X.P. Cui, *Appl. Surf. Sci.* 316, 549 (2014).
31. D.F. Hou, H.B. Ma, X.Y. Li, J.J. Chen, J. He, and H.W. Liao, *Polym. Mater. Sci. Eng.* 33, 48 (2017).

Publisher's Note Springer Nature remains neutral with regard to jurisdictional claims in published maps and institutional affiliations.